



Quantitative investigation on localized deformation process of rocks by uniaxial test and digital image correlation

Xiangjun Pei¹ · Shenghua Cui^{1,2} · Ling Zhu¹ · Luguang Luo^{1,3} · Jianlong Cheng¹ · Hui Wang¹ · Ruifeng Du¹ · Qingwen Yang¹

Received: 18 May 2022 / Accepted: 19 April 2023 / Published online: 17 May 2023
© The Author(s), under exclusive licence to Springer-Verlag GmbH Germany, part of Springer Nature 2023

Abstract

Determining the localized deformation mechanism is of vital importance to understand the failure processes of geomaterials in practical engineering. In this study, uniaxial monotonic and cyclic loading tests of slate samples were conducted and the failure processes were recorded by using the AE system and digital image correlation (DIC). The results show that the deformation field variance increases significantly in the initiation of the macro-scale failure stage. Under cyclic loading, the shape of the stress-variance hysteresis curve varies with increasing upper limit stress, and four types of stress-variance hysteresis curves were revealed. Increasing lag time of variance indicates gradual accumulation of damage to the sample. The comprehensive analysis of the evolution process of damage variables defined by cumulative AE counts and variance reveals that the rock failure process can be divided into crack closure stage, initial damage stage, stable development stage, accelerated development stage and failure stage. By proposing the differentiation rate, it is found that there are apparent failure precursor points under monotonic and cyclic loading.

Keywords Localized deformation · Digital image correlation · Deformation field variance · Damage accumulation

Introduction

Rock is typically characterized by heterogeneity, anisotropy and discontinuity, there are a large number of pores, fractures, schistosity, bedding and other defects. These defective structures determine the non-uniform damage and deformation localization of rock under loading (Erarslan and Williams 2012; Zhu et al. 2019). The deformation localization is the mechanism of microcrack initiation, propagation, coalescence and macrocrack development (Yuan and Harrison

2006; Ghasemi et al. 2021). Revealing the localized deformation process is of great significance to the stability assessment of rock slopes and underground chambers in active tectonic areas (Shen et al. 2014; Gischig et al. 2016; Zhu et al. 2021).

Many uniaxial and triaxial tests have been carried out to study the deformation evolution of rock under loading (Liu et al. 2014; Cerfontaine and Collin 2018; Fu et al. 2020; Yang et al. 2020; Zheng et al. 2020; Liu and Dai 2021). The rock damage evaluation methods based on residual strain,

✉ Shenghua Cui
cuishenghua18@cdut.edu.cn

Xiangjun Pei
peixj0119@tom.com

Ling Zhu
zhuling.cdut@gmail.com

Luguang Luo
luolgcdut@163.com

Jianlong Cheng
chengjl2018@foxmail.com

Hui Wang
wanghui1@stu.cdut.edu.cn

Ruifeng Du
494796853@qq.com

Qingwen Yang
yangqingwen1991@outlook.com

¹ State Key Laboratory of Geohazard Prevention and Geoenvironment Protection, Chengdu University of Technology, Chengdu 610059, China

² Disaster Prevention Research Institute, Kyoto University, Uji, Kyoto 6110011, Japan

³ University of Twente, Faculty of Geo-Information Science and Earth Observation (ITC), PO Box 217, 7500 AE Enschede, The Netherlands

elastic modulus, energy dissipation and acoustic emission (AE) signals were proposed (Antonaci et al. 2012; Liu and He 2012; Kim et al. 2015; Peng et al. 2019; Li et al. 2020). To deeply understand the deformation development process of rock under loading, various advanced monitoring technologies have been introduced, including holographic interference, AE, thermal infrared, computed tomography (CT), nuclear magnetic resonance imaging (NMRI) so on. Holographic interference technique could reveal the formation of permanent deformation under loading from the microscopic viewpoint of rock particle deformation, slip and loosening. The propagation process of microcracks in rocks during loading is revealed by obtaining AE parameters, including AE counts, dissipation energy, risetime/amplitude (RF) and average frequency (AR), and spectral features (Meng et al. 2018; Zhao et al. 2020). Monitoring the change of rock temperature under loading by thermal infrared can reveal the properties of initiated cracks and obtain the precursory information of rock failure (Cai et al. 2020; Cao et al. 2020). In addition, CT and NMR techniques were widely used to quantitatively evaluate the changes of pores and cracks in rocks (Feng et al. 2004; Xie et al. 2018; Wang et al. 2021). Although the above monitoring technologies have been widely used, monitoring and quantifying non-uniform damage and deformation localization during loading is difficult.

Digital image correlation (DIC) is an effective technology for full-field and real-time measurement of surface displacement and localization band of rock. It has been successfully applied to the observation of surface displacement of different rocks and test types. Huang et al. (2020) studied the crack initiation and propagation of tunnel sidewall under external loading and revealed that faults had an important impact on the stability of rock tunnels. Cheng et al. (2017) studied the deformation localization and crack propagation process of a series of composite rock samples with different dip angles. Liu et al. (2021) revealed the crack initiation process of granite with a single defect under uniaxial compression and identified three crack types with different initiation mechanisms by the DIC technique. Song et al. (2013) reported the whole process of crack propagation and coalescence in the sandstone through surface strain. Song et al. (2013) investigated the completed process from crack propagation to failure of sandstone through surface displacement. Zhang et al. (2020a) determined the crack formation and development process of rock samples with different geometric defects by deformation localization.

DIC technique has been widely used in rock mechanics tests. However, few studies involve the quantitative evaluation of deformation localization under monotonic and cyclic loading. In this paper, the variance of the surface deformation field is introduced, the characteristics of stress–strain and stress-variance curves are compared. The development process of the stress-variance hysteresis curve during

cyclic loading was investigated. Based on the AE counts and variance, the damage evolution process of the sample under cyclic loading was revealed. The differentiation rate of the deformation field is defined, and the evolution law of differentiation rate and the precursory failure information is analyzed. A new method for evaluating the deformation evolution of rock under loading is proposed in this paper.

Test method

Test scheme and instrument

The sample was taken from the same rock block in the slate of the Zagunao formation of the Triassic and cut into a cylinder with a diameter of 50 mm and a length of 100 mm. The preparation process strictly followed the standards of the international society of rock mechanics (ISRM). The slate was slightly weathered, and the mineral composition was analyzed by X-ray diffraction, and it was found that the slate was mainly composed of 48% quartz, 38% plagioclase, 5% chlorite and 10% clay minerals. Some fine and unevenly distributed quartz, sericite and other minerals could be seen from the microscope. The quartz was unevenly extinction due to stress. The minerals were mostly in the form of aggregates with obvious orientation, the quartz grain size was mainly distributed in 0.1–0.6 mm with coarse crystals, in addition to more cryptocrystals with obvious plastic deformation (Fig. 1). From the regional geological background of the sampling site, the slate was the product of low-level regional metamorphism, formed in a regional low-temperature power metamorphism with lower temperature and stronger stress. Monotonic and multi-level & multi-cycle loading uniaxial tests were carried out. The axial displacement rate of the monotonic loading uniaxial test was 0.1 mm/min. For the multi-level & multi-cycle loading uniaxial tests, the sine wave with a frequency of 0.5 Hz was used, and the minimum axial force was set to 1kN. The upper limit stress difference ratio between two adjacent stress levels was 0.05 and 30 cycles were performed at each stress level. The upper limit stress ratio of the first cyclic stress level was 30%. The upper limit stress applied in each one of the eight sets of 30 cycles was shown in Table 1. The monotonic loading was imposed at a loading rate of 1 kN/s after cyclic loading. The axial loading was set according to the stress path (Fig. 2) until the failure of the rock samples. Of which: σ_{\max} and σ_{\min} were the upper and lower limit stress respectively. σ_{amp} was the cyclic stress amplitude. σ_{st} was the stress difference between two adjacent stress levels.

The test was conducted on a MTS815 servo-controlled testing machine, which could apply a maximum axial force of 4600kN and a maximum axial strain of 5 mm. Micro-II AE instrument was used to monitor the fracture process of

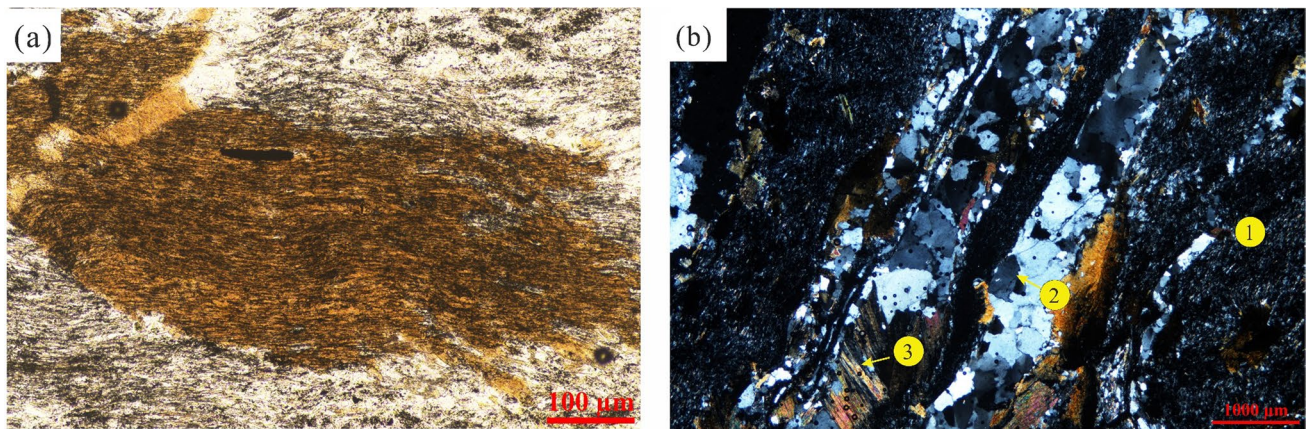


Fig. 1 Microstructure of slate, **a** single polarized light, **b** perpendicular polarized light. ① cryptocrystalline texture, ② quartz, ③ sericite

Table 1 Multi-level and multi-cycle loading test scheme

Sequence	Upper limit stress ratio	Upper limit stress (MPa)
①	0.30	11.97
②	0.36	13.96
③	0.42	16.01
④	0.48	17.96
⑤	0.54	20.08
⑥	0.60	22.26
⑦	0.66	24.30
⑧	0.72	26.32

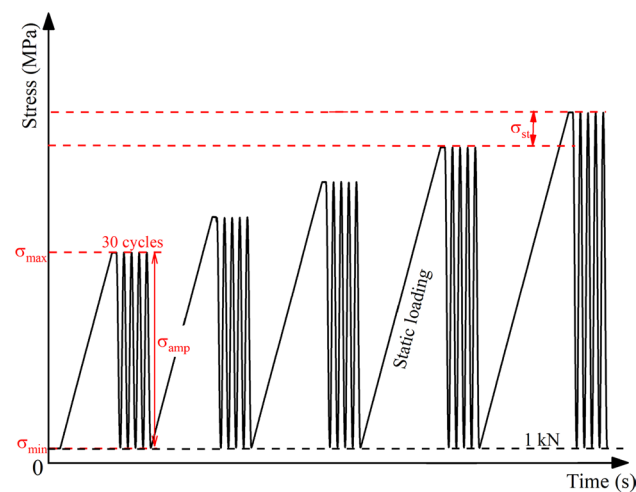


Fig. 2 The stress path of the multi-level and multi-cycle loading test

the sample in real-time (Fig. 3). The sampling threshold was 40 dB and the sampling interval was 1 μs. The monitoring frequency range of the AE sensor was 75–750 kHz.

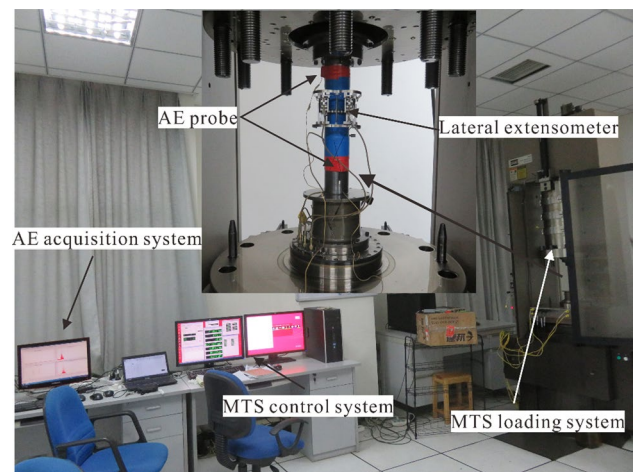
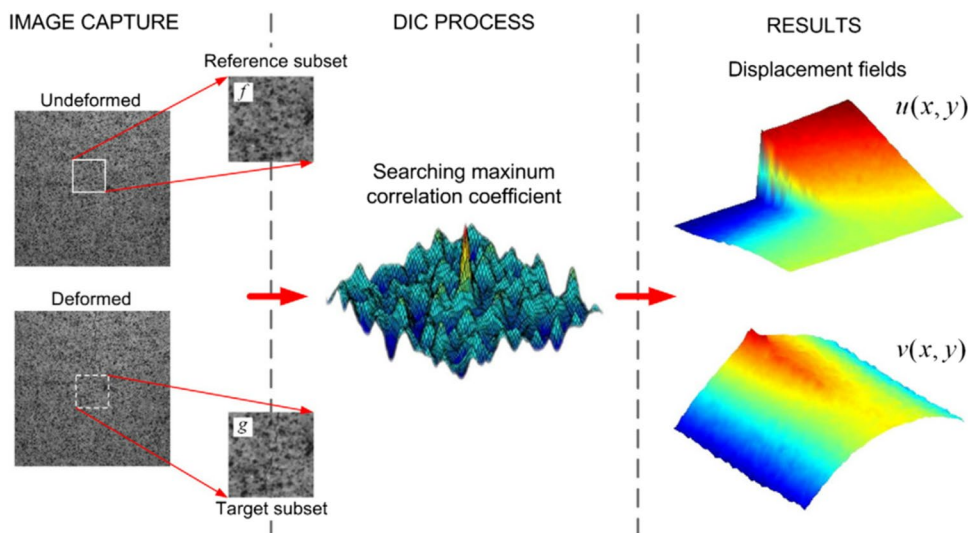


Fig. 3 MTS 815 rock mechanics test system, AE system and DIC system

DIC and variance of the deformation field

DIC is an optical measurement technique widely used in surface deformation measurement in rock mechanics (Munoz et al. 2016; Cao et al. 2018). As shown in Fig. 4, the principle of DIC is to match the square subset centered on a pixel based on the undeformed image and deformed image. The displacement is obtained by calculating the coordinate difference of the same pixel before and after deformation. The displacement field is determined by repeating this process. Song et al. (2013) reported that the correlation coefficient between the reference subset and the target subset was defined as follows:

Fig. 4 Schematic diagram of digital image correlation (Song et al. 2013)



$$C(X) = \frac{\sum_{i=1}^m \sum_{j=1}^m [f(x_i, y_i) - \bar{f}] \cdot [g(x_i^*, y_i^*) - \bar{g}]}{\sqrt{\sum_{i=1}^m \sum_{j=1}^m [f(x_i, y_j) - \bar{f}]^2 \cdot \sum_{i=1}^m \sum_{j=1}^m [g(x_i^*, y_j^*) - \bar{g}]^2}} \tag{1}$$

where $f(x, y)$ is the gray value of the reference image at coordinates (x, y) , $g(x^*, y^*)$ is the gray value of the target image at coordinates (x^*, y^*) , and f and g are the average values of functions $f(x, y)$ and $g(x^*, y^*)$ respectively.

The surface deformation measurement reveals that the rock sample has significant non-uniform deformation characteristics under loading. The non-uniform deformation will result in a localized deformation zone, which is different from the uniform deformation field. First, the deformation of a few pixel points is much greater than that of other pixel points. Second, these pixel points with large deformation are concentrated in one or a few connected bands (Yang et al. 2018). In mathematical statistics, variance is a measure of the dispersion degree in a group of data. The formation and development of deformation localization lead to a significant dispersion in a deformation field. Therefore, the variance is defined to quantify the dispersion degree of the deformation field. The calculation formula is as follows:

$$S_{\epsilon_i}^2 = \frac{1}{N-1} \sum_{i=1}^N (\epsilon_{ij} - \bar{\epsilon}_i)^2 \tag{2}$$

where $S_{\epsilon_i}^2$ is the variance of the deformation field in the i th time step, and N is the number of subsets. ϵ_{ij} is the i th time step deformation corresponding to the j th subset. $\bar{\epsilon}_i$ is the average value of the i th time step deformation field, which is defined as:

$$\bar{\epsilon}_i = \frac{1}{N} \sum_{j=1}^N \epsilon_{ij} \tag{3}$$

Test result

Monotonic loading test result

According to the stress–strain curve characteristics under monotonic loading, the rock deformation is divided into five stages in sequence, i.e., crack closure (stage I), elastic region (stage II), stable crack growth (stage III), initiation of macro-scale failure (stage IV) and global post-peak failure (stage V) (Huang et al. 2016) (Fig. 5a). The strength decreases rapidly after failure (σ_c : 43.34 MPa), showing apparent brittle failure characteristics. The axial strain corresponding to the peak strength is 0.72%. However, the variance under monotonic loading has no apparent increase in the crack closure stage, elastic region stage, stable crack growth stage, as shown in Fig. 5b. The evolution process of the variance can be divided into three stages. (i) Initial deformation stage, the variance increases slowly, There are no or few new microcracks, and the distribution of the deformation field is relatively uniform. (ii) Initiation of macro-scale failure stage, the variance begins to increase significantly. The shear crack initiates and propagates, and the angle between the loading direction and the shear crack is 45° . The shear crack propagates to the middle of the sample, and the tensile crack appears along the loading direction. Gradually, the crack coalescence occurs. (iii) Global post-peak failure stage, the stress falls instantaneously, after which the variance

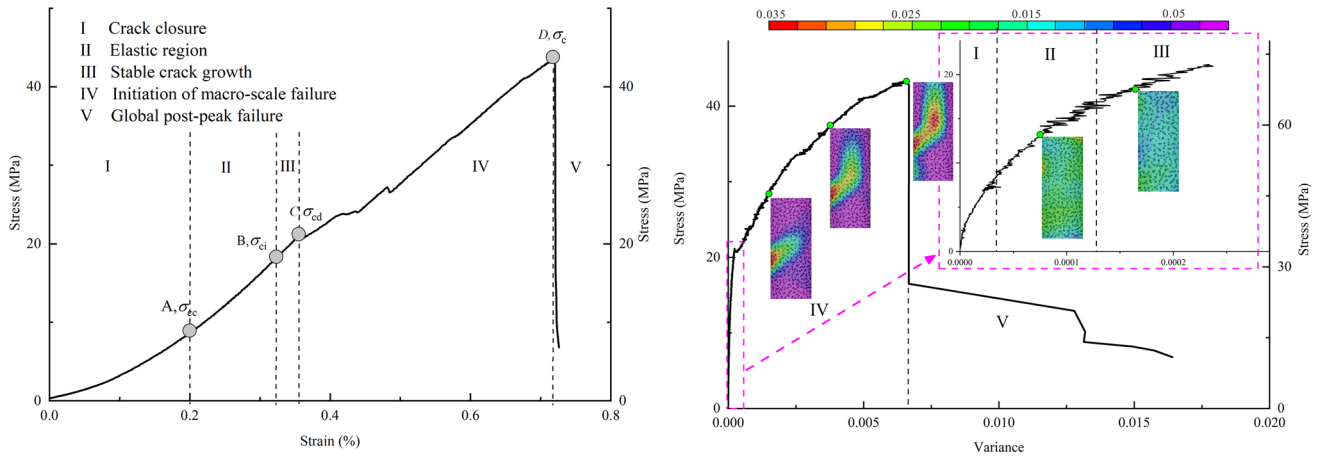


Fig. 5 Stress–strain and stress-variance curves

Table 2 Strain/variance ratio at different stages

Stage	Strain ratio(%)	Variance ratio(%)
Crack closure	27.22	1.14
Elastic region	17.48	5.79
Stable crack growth	5.65	6.30
Initiation of macro-scale failure	49.65	86.77

increases rapidly with decreasing stress, indicating the development of macroscopic cracks and the occurrence of failure to the sample. To reveal the development difference of strain and variance during loading, we proposed the strain/variance ratio (defined as the ratio of the strain/variance generated in each stage to the failure strain/variance). As shown in Table 2, the strain is mainly generated in the initiation of macro-scale failure stage (49.65%) and crack closure stage (27.22%). However, the variance is

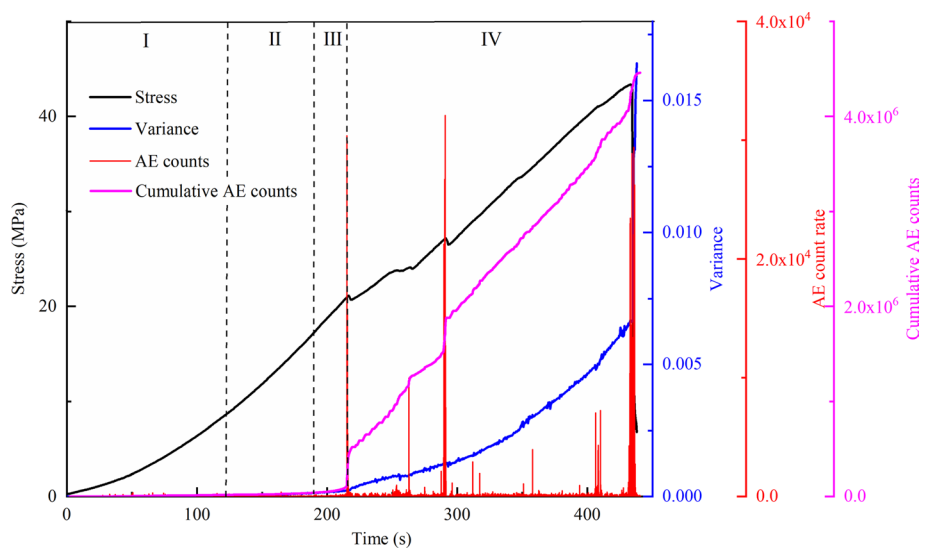
minimal in the crack closure stage, elastic region stage, stable crack growth stage, accounting for 13.23%. In the initiation of the macro-scale failure stage, the variance increases rapidly, accounting for 86.77%.

Figure 6 shows the time series data of the stress, variance, AE count rate and cumulative AE counts. From Fig. 6, the variance and cumulative AE counts increase barely in the crack closure stage, elastic region stage, stable crack growth stage, while the variance and cumulative AE counts increase significantly in the initiation of macro-scale failure stage. It is noted that the curves of the variance and cumulative AE counts show similar growth characteristics.

Cyclic loading test result

Figure 7 shows the stress–strain and stress-variance curves under multi-level & multi-cycle loading. The two curves show similarities and differences. The residual strain of the

Fig. 6 Time series data of the stress, variance, AE count rate and cumulative AE counts



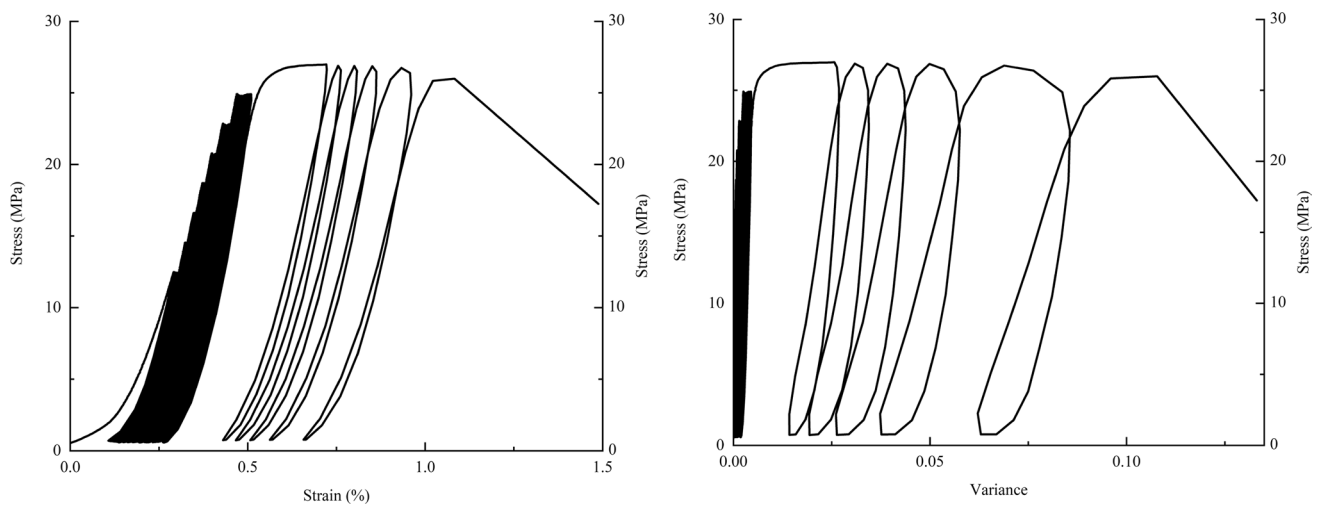


Fig. 7 Stress–strain and stress-variance curves

Table 3 Relationship between the correlation coefficient and correlation degree

Pearson correlation coefficient	Correlation degree
0	No correlation
0–0.3	Weak correlation
0.3–0.5	Low correlation
0.5–0.8	Median correlation
0.8–1	High correlation
1	Complete correlation

Table 4 Pearson correlation coefficient of axial strain and variance

Cyclic stress level	Pearson correlation coefficient (r)
①	0.95
②	0.97
③	0.91
④	0.76
⑤	0.54
⑥	0.26
⑦	0.46
⑧	0.61

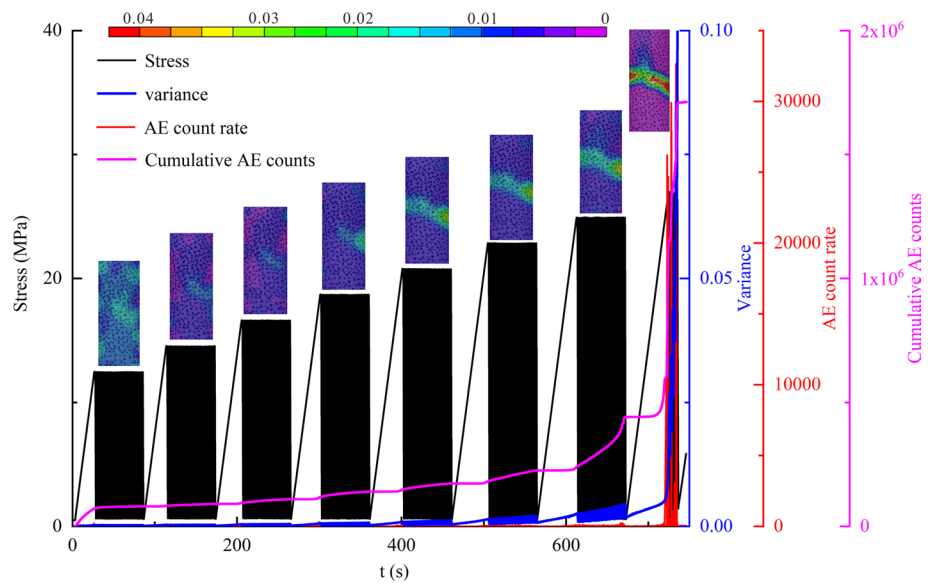
sample continuously develops with increasing upper limit stress, representing the damage accumulation. Similarly, the variance gradually accumulates under cyclic loading. At the eighth cyclic stress level, both the strain and variance increase rapidly. The sample was failed after applying the eighth cyclic stress level for five cycles. However, at the end of the seventh cyclic stress level, the total strain is 0.511%, about 47% of the failure strain (1.08%). In comparison, the total variance is 0.00445, which is only 4.13% of the failure variance (0.1078). This result reveals that the increase of variance mainly occurs at the eighth cycle stress level.

Pearson correlation coefficient, a statistical index describing the degree of correlation between different variables, is introduced to determine the correlation between axial strain and variance during cyclic loading. The absolute value of the Pearson correlation coefficient indicates the degree of correlation, as shown in Table 3. Table 4 shows the correlation coefficient of axial strain and variance at different stress levels. From Table 4, the correlation coefficient ranges from 0.26 to 0.97. In addition, there is a highly positive correlation between axial strain and variance in the first three cyclic stress levels. The correlation coefficient decreases

gradually with increasing upper limit stress. It is considered that the axial strain indicates the overall deformation, but the variance indicates the deformation localization. Before the obvious deformation localization, the axial strain is highly correlated with the variance. With the occurrence and progressive development of the localized deformation zone, the correlation decreases gradually, indicating that the axial strain can not show the process of localized deformation.

Figure 8 shows the contour of the deformation field and time-series data of stress, variance, AE count rate and cumulative AE counts under multi-level & multi-cycle loading. The contour shows that the deformation localization is progressively induced with raising upper limit cyclic stress. Comparing the deformation field contour under different cyclic stress levels, it is found that no obvious localized deformation zone appears in the first three cyclic stress levels. Afterwards, a significant localized deformation zone is formed. With increasing upper limit stress, the band expands and the deformation difference between the band and the adjacent area increases. Finally, the sample is failed along with the band at the

Fig. 8 Contour of the deformation field and time-series data of stress, variance, AE count rate and cumulative AE counts



eighth cyclic stress level. The variance increases significantly before sample failure, which is also the period of intensive AE signals. However, it is noted that the cumulative AE counts curve shows different development stages at the first seventh cyclic stress levels, which will be later discussed. The monotonic and cyclic loading test results also show similar characteristics. From the viewpoint of microscopic, the sample deformation in the initial period is attributed to pore and fissure closure, particle compression and a small number of microcracks. However, there is no obvious deformation localization band on the sample surface. Thus the variation of variance is tiny. After the deformation localization band is generated, the variance will sharply increase. The variance can accurately show the development process of the crack propagation and deformation localization band.

The amplitude distribution of AE can be described by the b value, which is a parameter representing the magnitude-frequency characteristic. The variation characteristic of the b value is helpful to understand the damage evolution process of samples. The b value can be obtained by (Gutenberg and Richter 1944):

$$\lg(N(A)) = C - b \lg(A) \tag{4}$$

where A is the amplitude of AE events, $N(A)$ is the total number of AE events greater than amplitude A . The increase of b value indicates that the small-scale microcracks are mainly generated in the sample, and the constant b value suggests that the scale distribution of the microcracks is relatively stable, and the decrease of b value indicates the increase of large-scale microcracks (Lockner et al. 1991).

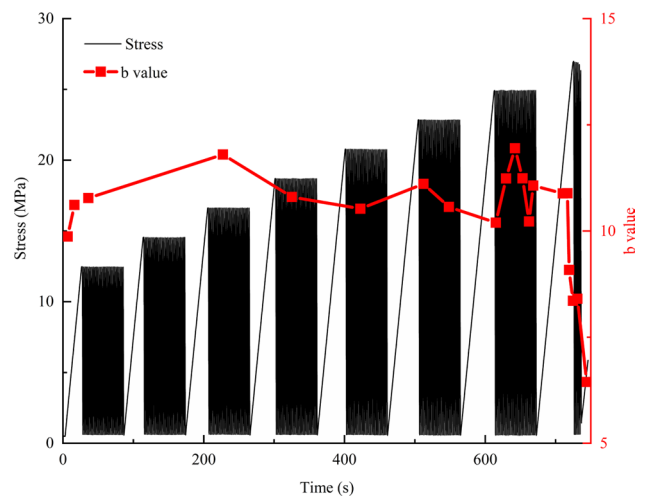


Fig. 9 Time series data of axial stress and b-value

The evolution process of the b value is shown in Fig. 9, the b value is large and stable at the first seven cyclic stress levels, indicating that the small-scale microcracks are mainly generated. The small change of the b value reveals a steady development of microcracks and a progressive damage process. Afterwards, the rapid decrease of the b value indicates that the large-amplitude AE events increase significantly and the macrocracks appear. This result shows that the microcracks propagation mainly occurs in the first seven cyclic stress levels, and macrocracks appear in the eighth cyclic stress level, which interprets the significant increase of variance at the eighth cyclic stress level.

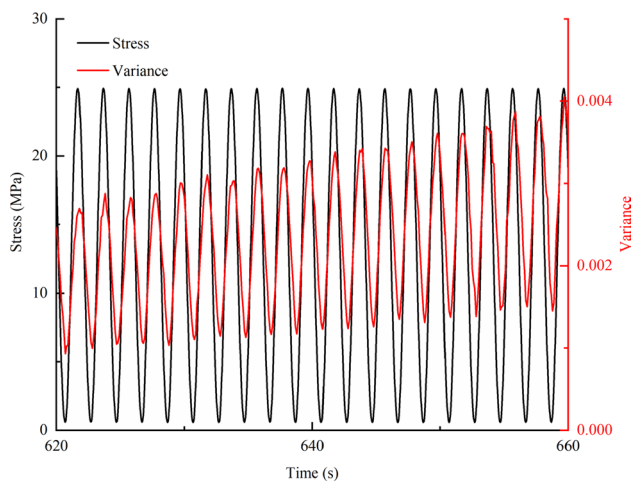


Fig. 10 Time series data of axial stress and variance

Result analysis

Variance response characteristics

Figure 10 shows the time series data of axial stress and variance. The variance varies with the cyclic stress, and the variance increases in the loading stage and decreases in the unloading stage. In addition, the total variance and residual variance rise gradually with growing cycles. As a natural geological material, rock has a large number of microcracks, pores and other inner defects. The microstructure characteristic of rock results in its nonlinear elastic behavior and significant hysteresis behavior (Chen et al. 2003; Li et al. 2019). The hysteresis curves of the stress–strain and stress–variance at different stress levels are shown in Fig. 11 and Fig. 12. At the first seven cyclic stress levels, the strain phase

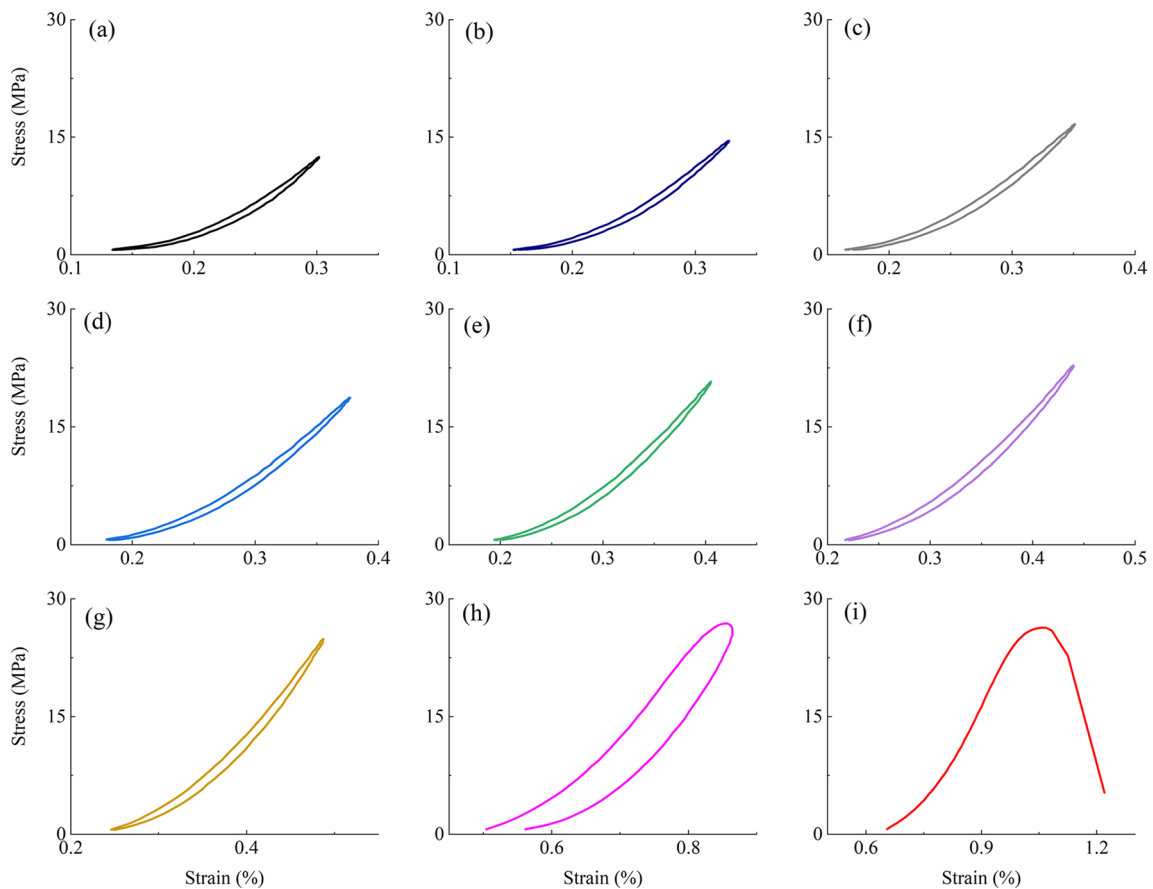


Fig. 11 Stress–strain hysteresis curves, **a** 15th cycle (first stress level), **b** 45th cycle (second stress level), **c** 75th cycle (third stress level), **d** 105th cycle (fourth stress level), **e** 135th cycle (fifth stress

level), **f** 165th cycle (sixth stress level), **g** 195th cycle (seventh stress level), **h** 212 cycle (eighth stress level), **i** 215th cycle (eighth stress level)

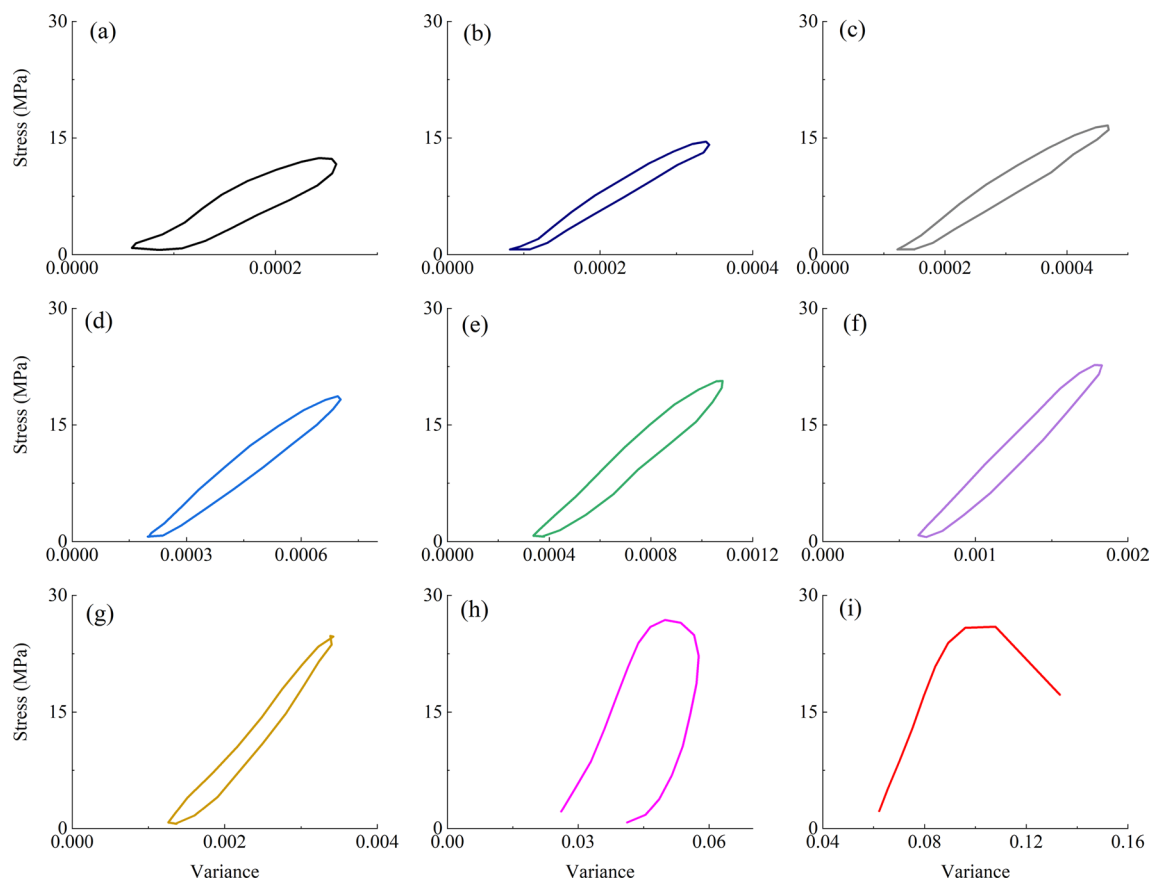


Fig. 12 Stress- variance hysteresis curves, **a** 15th cycle (first stress level), **b** 45th cycle (second stress level), **c** 75th cycle (third stress level), **d** 105th cycle (fourth stress level), **e** 135th cycle (fifth stress

level), **f** 165th cycle (sixth stress level), **g** 195th cycle (seventh stress level), **h** 212 cycle (eighth stress level), **i** 215th cycle (eighth stress level)

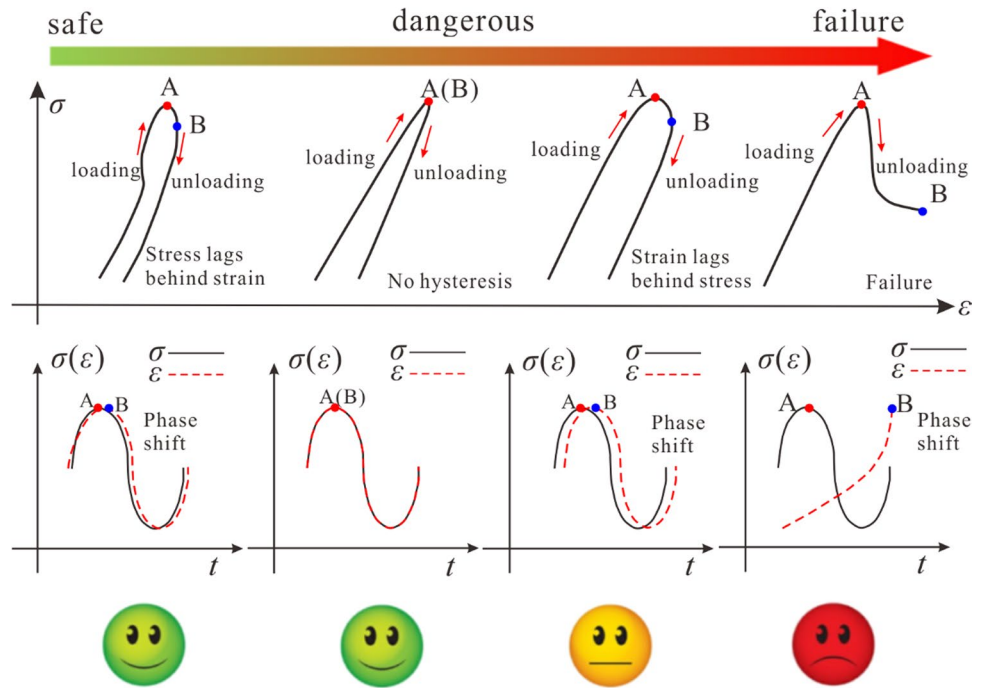
continually advances the stress phase at the loading stage, and the stress–strain hysteresis curves are crescent. However, the variance phase changes from advancing to lagging stress phase at the first three stress levels, the stress-variance hysteresis curves are long eggplant. Gradually, the variance phase lags behind the stress phase, and the hysteresis curves become oval. At the eighth stress level, the shape of the stress–strain and stress-variance hysteresis curves is similar. The hysteresis curves are not closed, indicating significant residual strain/variance is induced in the sample.

Based on the above findings, the types of stress-variance hysteresis curves under multi-level & multi-cycle loading were summarized. As shown in Fig. 13. Point A and point B are the maximum stress point and the maximum variance point respectively. According to the characteristic of the hysteresis curve, the evolution process of the hysteresis curve is revealed. If the variance phase changes from advancing to lagging stress phase, point B lags behind point A and the hysteresis curve is long eggplant, it indicates that the deformation induced by crack closure is dominant. When point A and point B appear at

the same time or point B lags behind briefly, the hysteresis curves are oval. The sample shows good elastic behavior and there are no extensive cracks in the sample. The lag time of point B increases, indicating the gradual damage accumulation. A longer lag time means a higher failure potential (Tutuncu et al. 1998; Song et al. 2018, 2021). Figure 14 shows the relationship between the lag time of point B and cyclic stress level. It can be seen that the variation characteristic of the average lag time of strain and variance is the same. The lag time increases suddenly at the eighth cyclic stress level, which reveals that the sample's damage degree and failure potential increases sharply.

The "lag ratio" is defined as the ratio of the number of cycles with "strain/variance lag" to the total number of cycles at each cycle stress level. The total number of cycles for each stress level in this test is 30. Song et al. (2021) reported that the increase of the "lag ratio" presented the gradual increase of the failure potential. Figure 15 shows the evolution characteristics of the "lag ratio" of axial strain and variance. The "lag ratio" of variance increases with increasing upper limit stress, and there is a linear relationship

Fig. 13 Different types of stress-variance hysteresis during cyclic loading (modified from Zhang et al. 2020c)



between the "lag ratio" and the stress level. However, the "lag ratio" of axial strain increases significantly only at the eighth stress level. It is revealed that the "lag ratio" of axial strain presents insignificant response of the damage accumulation and the sudden increase of the failure potential. However, the "lag ratio" of variance reveals the progressive increase of failure potential.

Damage evolution characteristics

Figure 16 shows the relationship between residual variance, residual strain and cycle at each stress level. From

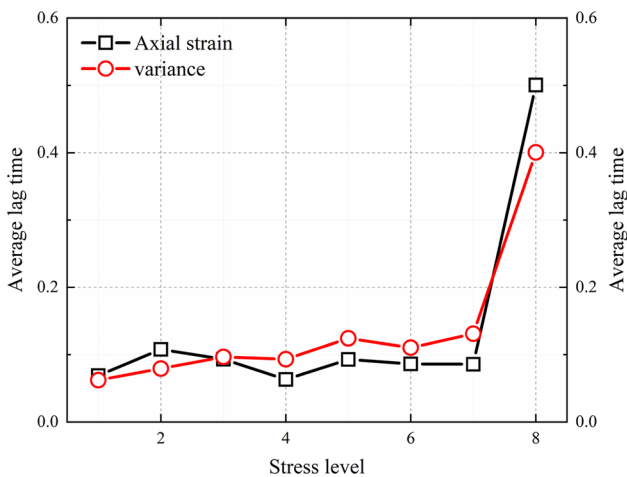


Fig. 14 Average lag time versus stress level

Fig. 16, the residual variance increases linearly with increasing cycles at the first seven cyclic stress levels. However, the rising rate of the residual strain decreases gradually at the first three cyclic stress levels. The scatters of residual strain and cycle are fitted by a logarithmic function. Afterwards, the residual strain increases linearly with increasing cycles. At the eighth cyclic stress level, the residual variance and residual strain increase exponentially with increasing cycles, and the sample is failed. The development of residual variance and residual strain under cyclic loading shows the same law except in the first three cyclic stress levels, which is attributed to the crack closure. The test time was very short when the sample was close to failure, so only a small amount of test data was collected, however, we conducted tests on three samples and all demonstrated the same pattern.

AE and deformation field variance data were used to quantitatively evaluate the rock damage evolution. Damage variables are respectively defined from internal and external damage by cumulative AE counts and variance. Liu et al. (2009) have derived the analytical expression of damage variable based on cumulative AE counts, but there are few studies on the expression of damage variable based on variance.

The damage variable based on cumulative AE counts can be defined as:

$$D_{AE} = D_u \frac{C_d}{C_0} = \left(1 - \frac{\sigma_c}{\sigma_p}\right) \frac{C_d}{C_0} \tag{5}$$

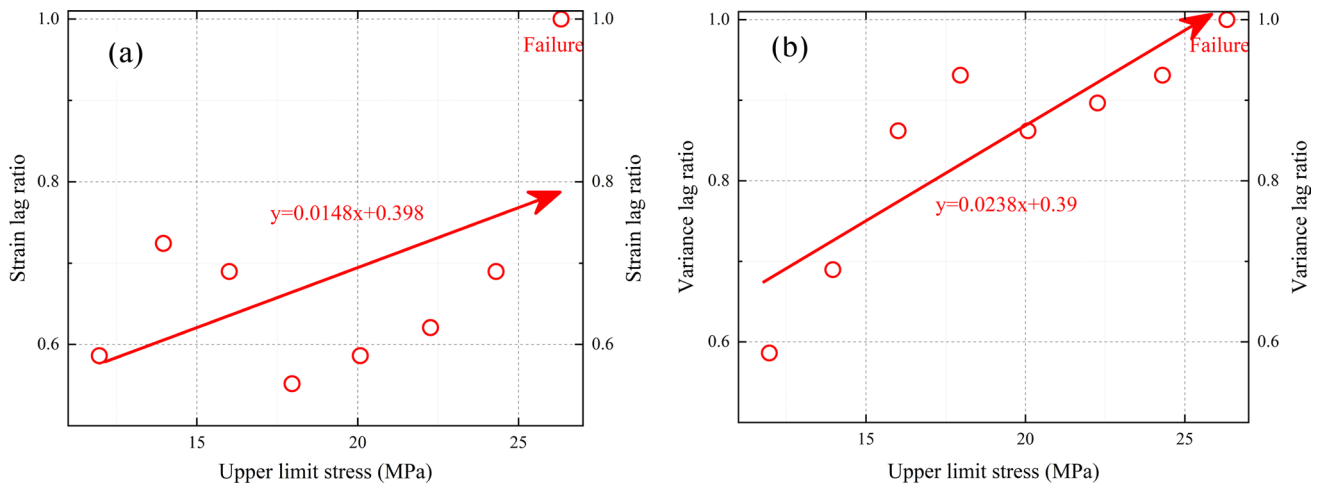


Fig. 15 Evolution of axial strain “lag ratio” versus stress level (a), the evolution of variance “lag ratio” versus stress level (b)

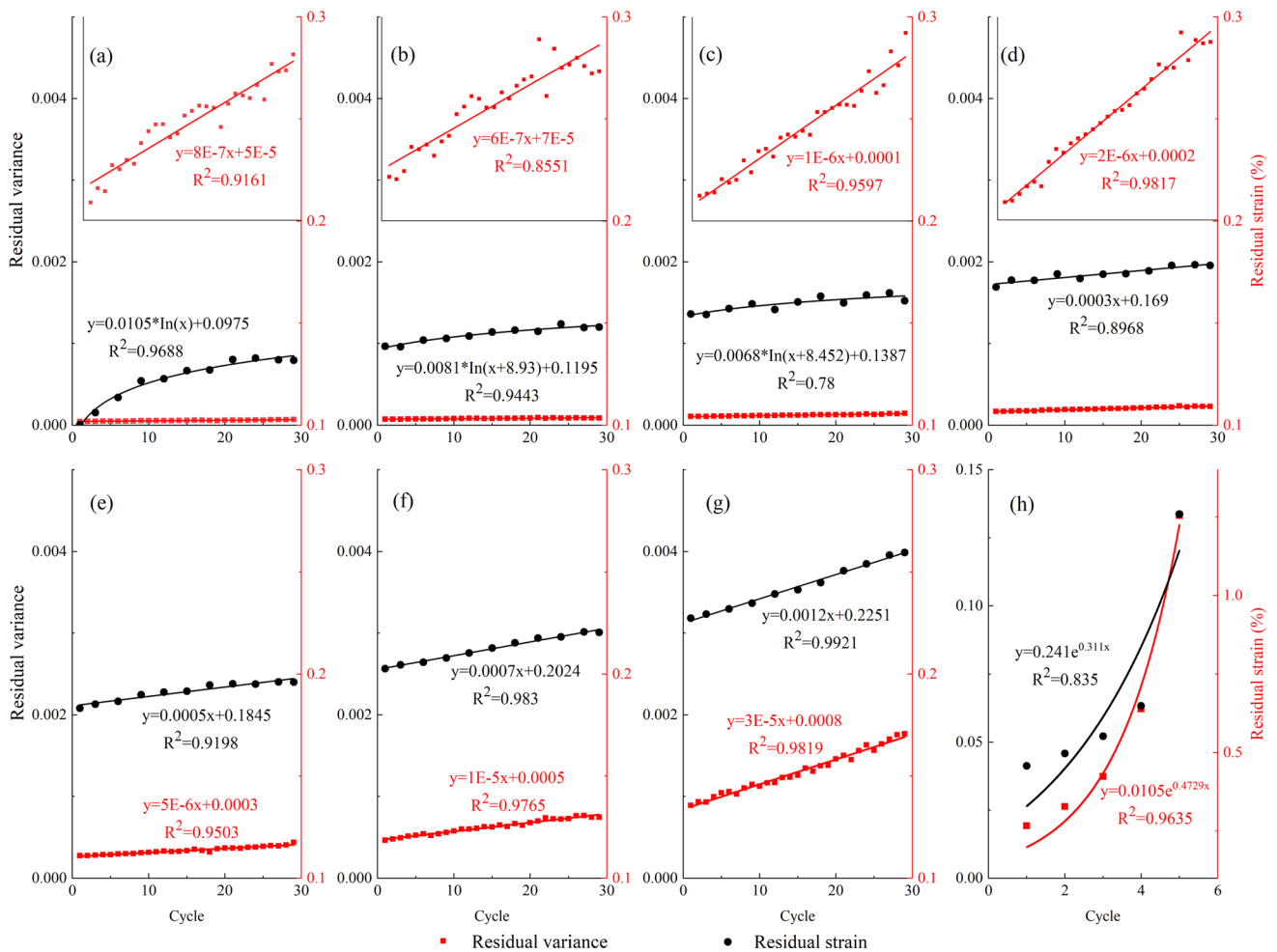


Fig. 16 Residual stain and residual variance versus cycle curves, a first stress level, b second stress level, c third stress level, d fourth stress level, e fifth stress level, f sixth stress level, g seventh stress level, h eighth stress level, i eighth stress level

where D_u is the critical damage; C_d is the cumulative AE counts at any time in the process of rock deformation; C_0 is the cumulative AE counts when the damage variable is D_u ; σ_c is the residual strength; σ_p is the peak strength.

The deformation localization is induced by the propagation and coalescence of microcracks and the formation of macrocracks. The variance can be used as a parameter to quantify the damage evolution of rock.

Damage variable D can be obtained by:

$$D = A_d/A \tag{6}$$

where A_d is the damaged area, A is the cross-section area of the undamaged sample.

V_0 is defined as the variance when the whole section of the sample is failed. The variance V_w induced by micro-unit damage in the unit area, V_w can be written as:

$$V_w = \frac{V_0}{A} \tag{7}$$

When the damaged area reaches A_d , the variance, V_d , can be expressed as:

$$V_d = V_w A_d = \frac{V_0}{A} A_d \tag{8}$$

Therefore, damage variable D_{VA} can be written as:

$$D_{VA} = \frac{V_d}{V_0} \tag{9}$$

In the rock mechanics test, the loading process will be terminated when the sample is not completed failed. The damage variable D_{VA} cannot reach 1, the D_{VA} is revised as (Cao et al. 2019):

$$D_{VA} = D_u \frac{V_d}{V_0} \tag{10}$$

where D_u is the critical damage variable.

D_u can be described as:

$$D_u = 1 - \frac{\sigma_c}{\sigma_p} \tag{11}$$

Therefore, the damage variable D_{VA} can be re-written as:

$$D_{VA} = \left(1 - \frac{\sigma_c}{\sigma_p}\right) \frac{V_d}{V_0} \tag{12}$$

Based on the characteristics of the D_{AE} and D_{VA} , the evolution process can be divided into five stages (Fig. 17): (i) Crack closure stage, the D_{VA} does not increase, and D_{AE} increases obviously, which is attributed to a lot AE counts induced by crack and pore closure. (ii) Initial damage stage,

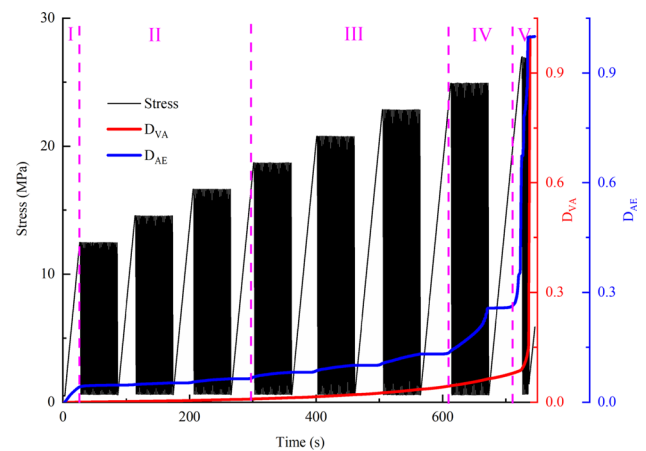


Fig. 17 Axial stress and damage variable versus time curves

the slopes of D_{AE} and D_{VA} approach 0, which means that few new microcracks are generated in this stage. (iii) Stable development stage, the D_{AE} and D_{VA} increase slowly with increasing cycles, indicating the generation and continuous propagation of the microcracks. (iv) Accelerated development stage, the increase of D_{AE} and D_{VA} is gradually accelerated, indicating the initiation, propagation and coalescence of a large number of microcracks. (v) Failure stage, the D_{AE} and D_{VA} increase significantly and the sample is failed in this stage. In addition, it is noted that the sudden increase of D_{AE} is earlier than that of D_{VA} , indicating that the significant damage first appears in the interior of the sample. Afterwards, the gradual development of internal cracks induced the surface deformation localization, macrocracks and the obvious increase of D_{VA} .

Failure precursory characteristic

The development characteristic of AE parameters and waveform under loading conditions can indicate the damage evolution process of rock. Generally, the spectrum characteristics obtained from the AE waveform can comprehensively describe the development process of microcracks (Fan et al. 2020). Therefore, the evolution feature of the AE spectrum in the process of rock fracture is investigated, and the failure mechanism and capture the precursor points of rock failure is revealed. In this paper, the peak frequency of the recorded AE waveform is obtained by fast Fourier transform. As shown in Fig. 18. Based on the distribution feature of peak frequency, the ranges of low, medium, high peak frequencies are divided into 40–128 kHz, 128–256 kHz and 256–500 kHz respectively.

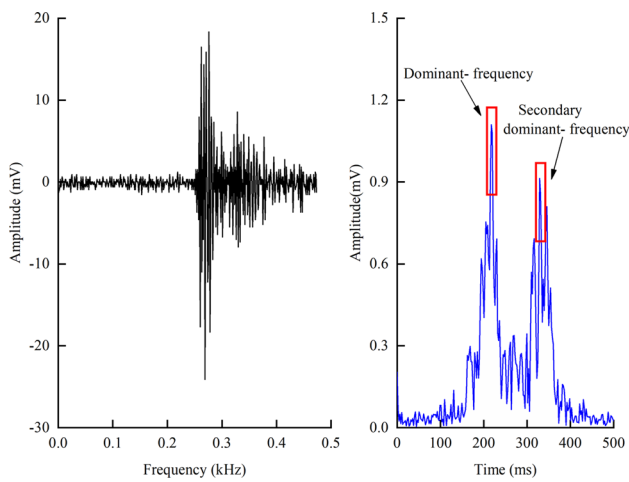


Fig. 18 Waveform and spectrum of AE signal

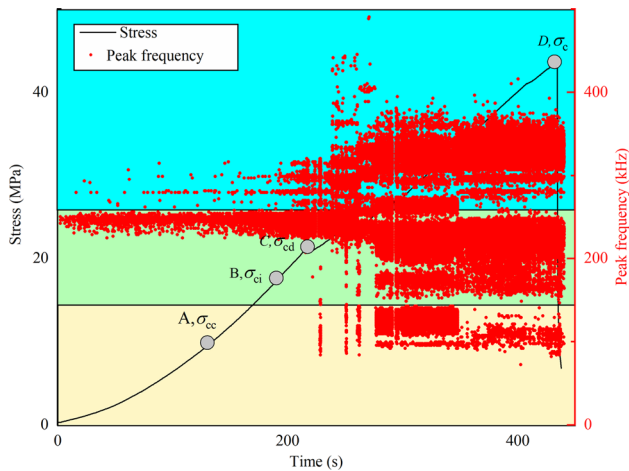


Fig. 19 Time series data of the stress, peak frequency under monotonic loading

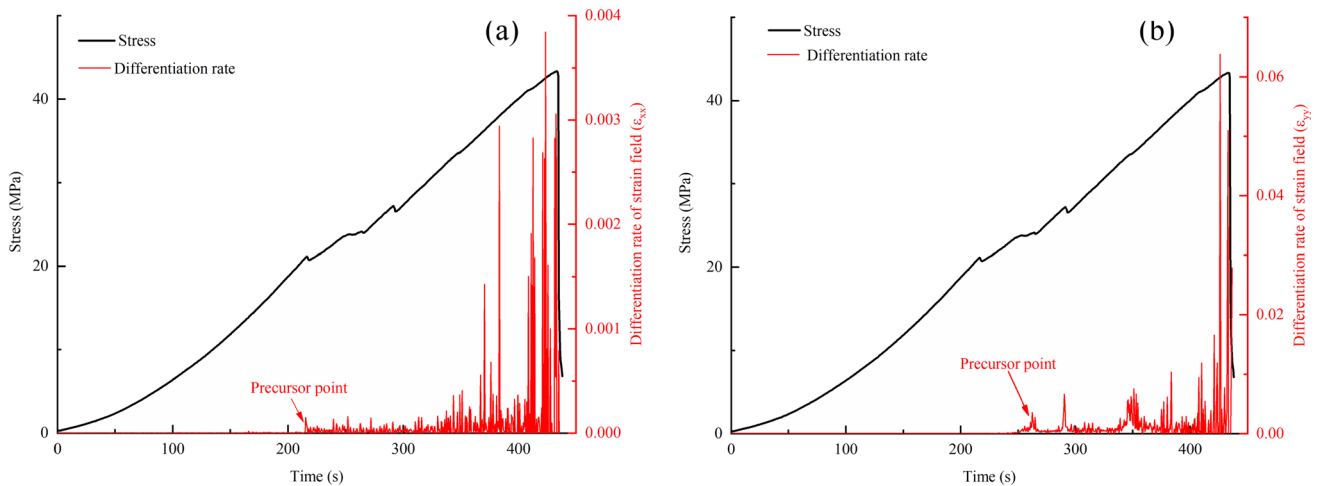


Fig. 20 Evolution of the differentiation rate under static loading, a ϵ_{xx} , b ϵ_{yy}

The variance has undergone a variation process from slow growth to rapid growth. To quantitatively describe the variation rate of the deformation field, the differentiation rate is obtained by the derivative of the variance with respect to the axial strain, the formula is as follows (Zhang et al. 2020b),

$$v_{\epsilon} = \frac{\partial S_{\epsilon,i}^2}{\partial \epsilon} \approx \frac{S_{\epsilon,i+1}^2 - S_{\epsilon,i-1}^2}{2\Delta\epsilon} \quad (13)$$

Figure 19 shows the time series data of the stress, peak frequency under monotonic loading. It is found that the distribution range of peak frequency depends on the deformation stage. In the crack closure stage, elastic region stage and stable crack growth stage, the peak frequency ranges from 228 to 278 kHz. However, in the initiation of the macro-scale failure stage, the peak frequency ranges from 95 to 445 kHz, and the distribution range of peak frequency is expanded. Figure 20 shows the horizontal and vertical differentiation rate (ϵ_{xx} and ϵ_{yy}) under monotonic loading. The horizontal and vertical differentiation rates approach 0 in the crack closure, elastic region, and stable crack growth stages. However, the obvious precursor points appear in the initiation of the macro-scale failure stage. The horizontal and vertical differentiation rate curves show similar development characteristics.

Figure 21 shows the time series data of the stress, peak frequency under cyclic loading. From Fig. 21, the wide distribution range of peak frequency is presented in the initial loading stage due to the fast loading rate. In addition, the distribution range of peak frequency is relatively stable compared with the static uniaxial test, and there is no obvious expansion of the distribution range of peak frequency with increasing upper limit stress. We believe that the multi-level and multi-cycle loading results in progressive damage and crack propagation process, thus no obvious precursor

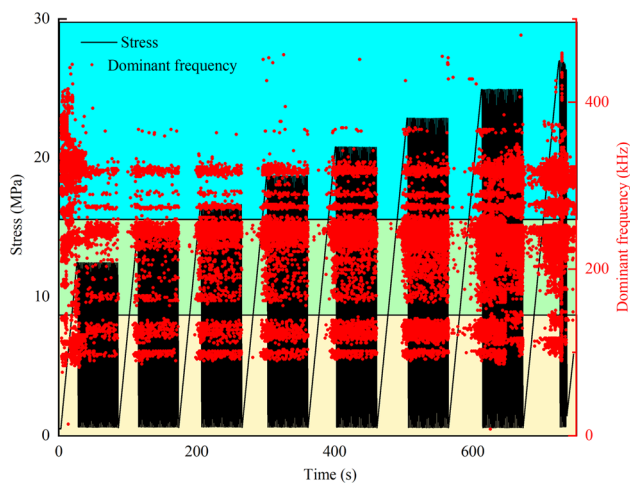


Fig. 21 Time series data of the stress, peak frequency under cyclic loading

formation based on AE spectrum is obtained under cyclic loading. In addition, the variation curves of the horizontal and vertical differentiation rate (ϵ_{xx} and ϵ_{yy}) under cyclic loading is obtained. As shown in Fig. 22, the horizontal and vertical differentiation rates approach 0 in the first seven cyclic stress levels. However, the obvious precursor points appear in the eighth cyclic stress level. Therefore, it is clear that the failure precursor point under cyclic loading can be obtained by differentiation rate.

At present, the failure precursory point is often obtained by analyzing AE parameters and spectrum. The peak frequency and differentiation rate under static loading show the apparent failure precursory point. However, there is always

progressive crack propagation and energy dissipation during cyclic loading, thus it is poor to reveal the failure precursor point based on the peak frequency. However, the variance has a high susceptibility after the local fracture band appears, and the differentiation rate of variance can obtain the precursory point.

Conclusion

1. The variance begins to increase significantly in the initiation of macro-scale failure stage under monotonic loading, and it increases sharply under cyclic loading before sample failure.
2. In the initial stage, the stress-variance hysteresis curve is long eggplant, which indicates that the deformation induced by crack closure is dominant. Gradually, the hysteresis curves are oval. The sample shows good elastic behavior and there are no extensive cracks in the sample. The lag time of variance increases, indicating the gradual damage accumulation. A longer lag time indicates a higher failure potential
3. According to the evolution characteristics of the damage variable, the evolution process of damage variable can be divided into the crack closure stage, initial damage stage, stable development stage, accelerated development stage and failure stage.
4. The differentiation rate is proposed to reveal the failure precursory point under monotonic and cyclic loading. Compared with the characteristic of the AE spectrum, the curves of differentiation rate show obvious precursor points under cyclic loading.

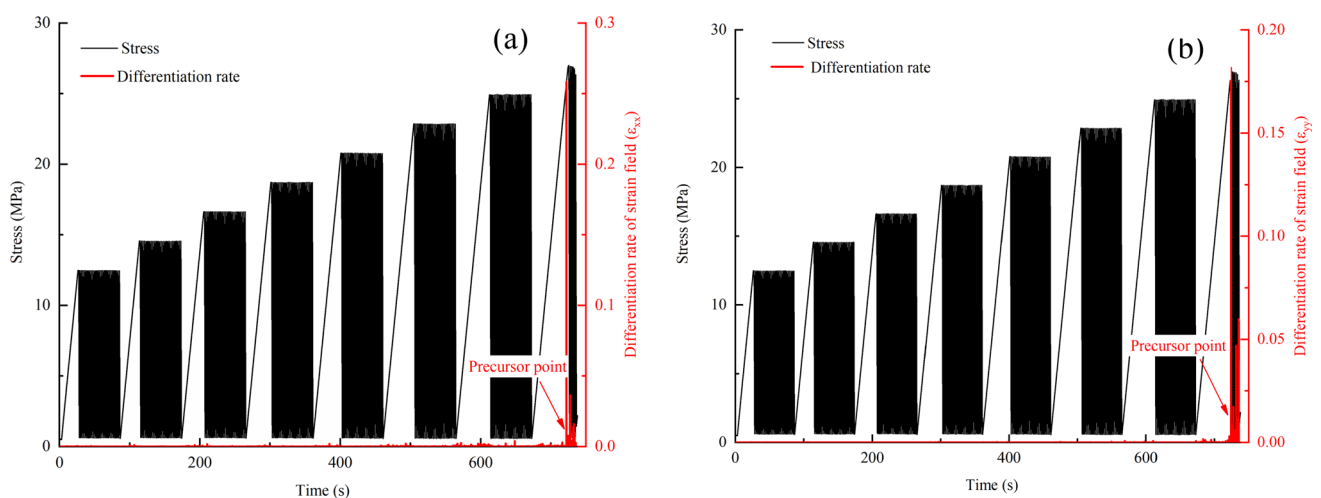


Fig. 22 Evolution of the differentiation rate for the deformation field under cyclic loading, **a** ϵ_{xx} , **b** ϵ_{yy}

Acknowledgements This study was financially sponsored by the National Natural Science Foundation of China (Grant No. 41931296), the National Key R&D Program of China (No. 2017YFC1501002) and the National Nature Science Foundation of China (Grant Nos. 41907254 and 41521002).

Funding This research was funded by Key Programme, Grant no [41931296], National Key R&D Program of China, Grant no [2017YFC1501002], Young Scientists Fund, Grant no [41907254], National Natural Science Foundation of China, Grant no [41521002].

Data availability All data generated or analyzed during this study are included in this article.

Declarations

Conflict of interest The authors declare that they have no known competing financial interests or personal relationships that could have appeared to influence the work reported in this paper.

References

- Antonaci P, Bocca P, Masera D (2012) Fatigue crack propagation monitoring by acoustic emission signal analysis. *Eng Fract Mech* 81:26–32. <https://doi.org/10.1016/j.engfracmech.2011.09.017>
- Cai X, Zhou Z, Tan L, Zang H, Song Z (2020) Water saturation effects on thermal infrared radiation features of rock materials during deformation and fracturing. *Rock Mech Rock Eng* 53(11):4839–4856. <https://doi.org/10.1007/s00603-020-02185-1>
- Cao R, Lin H, Cao P (2018) Strength and failure characteristics of brittle jointed rock-like specimens under uniaxial compression: digital speckle technology and a particle mechanics approach. *Int J Min Sci Technol* 28(4):669–677. <https://doi.org/10.1016/j.ijmst.2018.02.002>
- Cao A, Jing G, Ding YL, Liu S (2019) Mining-induced static and dynamic loading rate effect on rock damage and acoustic emission characteristic under uniaxial compression. *Saf Sci* 116:86–96. <https://doi.org/10.1016/j.ssci.2019.03.003>
- Cao K, Ma L, Zhang D, Lai X, Zhang Z, Khan NM (2020) An experimental study of infrared radiation characteristics of sandstone in dilatancy process. *Int J Rock Mech Min Sci* 136:104503. <https://doi.org/10.1016/j.ijrmms.2020.104503>
- Cerfontaine B, Collin F (2018) Cyclic and fatigue behaviour of rock materials: review, interpretation and research perspectives. *Rock Mech Rock Eng* 51(2):391–414. <https://doi.org/10.1007/s00603-017-1337-5>
- Chen Y, Xi D, Xue Y (2003) Stress-strain dynamic response of saturated rocks under cyclic loading. *Oil Geophys Prospect* 38(4):409–413. [https://doi.org/10.13810/j.cnki.issn.1000-7210.2003.04.014\(inChinese\)](https://doi.org/10.13810/j.cnki.issn.1000-7210.2003.04.014(inChinese))
- Cheng JL, Yang SQ, Chen K, Ma D, Li FY, Wang LM (2017) Uniaxial experimental study of the acoustic emission and deformation behavior of composite rock based on 3D digital image correlation (DIC). *Acta Mech Sin* 33(6):999–1021. <https://doi.org/10.1007/s10409-017-0706-3>
- Erarslan N, Williams DJ (2012) Mechanism of rock fatigue damage in terms of fracturing modes. *Int J Fatigue* 43:76–89. <https://doi.org/10.1016/j.ijfatigue.2012.02.008>
- Fan X, Li S, Chen X, Liu S, Guo Y (2020) Fracture behaviour analysis of the full-graded concrete based on digital image correlation and acoustic emission technique. *Fatigue Fract Eng Mater Struct* 43(6):1274–1289. <https://doi.org/10.1111/ffe.13222>
- Feng XT, Chen S, Zhou H (2004) Real-time computerized tomography (CT) experiments on sandstone damage evolution during triaxial compression with chemical corrosion. *Int J Rock Mech Min Sci* 41(2):181–192. [https://doi.org/10.1016/S1365-1609\(03\)00059-5](https://doi.org/10.1016/S1365-1609(03)00059-5)
- Fu B, Hu L, Tang C (2020) Experimental and numerical investigations on crack development and mechanical behavior of marble under uniaxial cyclic loading compression. *Int J Rock Mech Min Sci* 130:104289. <https://doi.org/10.1016/j.ijrmms.2020.104289>
- Ghasemi S, Khamsehchiyan M, Taheri A, Nikudel MR, Zalooli A (2021) Microcracking behavior of gabbro during monotonic and cyclic loading. *Rock Mech Rock Eng* 54(5):2441–2463. <https://doi.org/10.1007/s00603-021-02381-7>
- Gischig V, Preisig G, Eberhardt E (2016) Numerical investigation of seismically induced rock mass fatigue as a mechanism contributing to the progressive failure of deep-seated landslides. *Rock Mech Rock Eng* 49(6):2457–2478. <https://doi.org/10.1007/s00603-015-0821-z>
- Gutenberg B, Richter CF (1944) Frequency of earthquakes in California. *Bull Seismol Soc Am* 34(4):185–188. <https://doi.org/10.1785/BSSA0340040185>
- Huang D, Gu D, Yang C, Huang R, Fu G (2016) Investigation on mechanical behaviors of sandstone with two preexisting flaws under triaxial compression. *Rock Mech Rock Eng* 49(2):375–399. <https://doi.org/10.1007/s00603-015-0757-3>
- Huang F, Wu C, Ni P, Wan G, Zheng A, Jang BA, Karekal S (2020) Experimental analysis of progressive failure behavior of rock tunnel with a fault zone using non-contact DIC technique. *Int J Rock Mech Min Sci* 132:104355. <https://doi.org/10.1016/j.ijrmms.2020.104355>
- Kim JS, Lee KS, Cho WJ, Choi HJ, Cho GC (2015) A comparative evaluation of stress-strain and acoustic emission methods for quantitative damage assessments of brittle rock. *Rock Mech Rock Eng* 48(2):495–508. <https://doi.org/10.1007/s00603-014-0590-0>
- Li T, Pei X, Wang D, Huang R, Tang H (2019) Nonlinear behavior and damage model for fractured rock under cyclic loading based on energy dissipation principle. *Eng Fract Mech* 206:330–341. <https://doi.org/10.1016/j.engfracmech.2018.12.010>
- Li T, Pei X, Guo J, Meng M, Huang R (2020) An energy-based fatigue damage model for sandstone subjected to cyclic loading. *Rock Mech Rock Eng* 53(11):5069–5079. <https://doi.org/10.1007/s00603-020-02209-w>
- Liu Y, Dai F (2021) A review of experimental and theoretical research on the deformation and failure behavior of rocks subjected to cyclic loading. *J Rock Mech Geotech Eng* 13(5):1203–1230. <https://doi.org/10.1016/j.jrmge.2021.03.012>
- Liu E, He S (2012) Effects of cyclic dynamic loading on the mechanical properties of intact rock samples under confining pressure conditions. *Eng Geol* 125:81–91. <https://doi.org/10.1016/j.enggeo.2011.11.007>
- Liu B, Huang J, Wang Z, Liu L (2009) Study on damage evolution and acoustic emission character of coal-rock under uniaxial compression. *Chin J Rock Mech Eng* 28(S1):3234–3238. <https://doi.org/10.3321/j.issn:1000-6915.2009.z1.096>. (In Chinese)
- Liu J, Xie H, Hou Z, Yang C, Chen L (2014) Damage evolution of rock salt under cyclic loading in uniaxial tests. *Acta Geotech* 9(1):153–160. <https://doi.org/10.1007/s11440-013-0236-5>
- Liu L, Li H, Li X, Wu D, Zhang G (2021) Underlying mechanisms of crack initiation for granitic rocks containing a single pre-existing flaw: Insights from digital image correlation (DIC) analysis. *Rock Mech Rock Eng* 54(2):857–873. <https://doi.org/10.1007/s00603-020-02286-x>

- Lockner D, Byerlee JD, Kuksenko V, Ponomarev A, Sidorin A (1991) Quasi-static fault growth and shear fracture energy in granite. *Nature* 350(6313):39–42. <https://doi.org/10.1038/350039a0>
- Meng Q, Zhang M, Han L, Pu H, Chen Y (2018) Acoustic emission characteristics of red sandstone specimens under uniaxial cyclic loading and unloading compression. *Rock Mech Rock Eng* 51(4):969–988. <https://doi.org/10.1007/s00603-017-1389-6>
- Munoz H, Taheri A, Chanda EK (2016) Pre-peak and post-peak rock strain characteristics during uniaxial compression by 3D digital image correlation. *Rock Mech Rock Eng* 49(7):2541–2554. <https://doi.org/10.1007/s00603-016-0935-y>
- Peng K, Zhou J, Zou Q, Zhang J, Wu F (2019) Effects of stress lower limit during cyclic loading and unloading on deformation characteristics of sandstones. *Constr Build Mater* 217:202–215. <https://doi.org/10.1016/j.conbuildmat.2019.04.183>
- Shen Y, Gao B, Yang X, Tao S (2014) Seismic damage mechanism and dynamic deformation characteristic analysis of mountain tunnel after Wenchuan earthquake. *Eng Geol* 180:85–98. <https://doi.org/10.1016/j.enggeo.2014.07.017>
- Song H, Zhang H, Kang Y, Huang G, Fu D, Qu C (2013) Damage evolution study of sandstone by cyclic uniaxial test and digital image correlation. *Tectonophysics* 608:1343–1348. <https://doi.org/10.1016/j.tecto.2013.06.007>
- Song Z, Konietzky H, Frühwirt T (2018) Hysteresis energy-based failure indicators for concrete and brittle rocks under the condition of fatigue loading. *Int J Fatigue* 114:298–310. <https://doi.org/10.1016/j.ijfatigue.2018.06.001>
- Song Z, Wang Y, Konietzky H, Cai X (2021) Mechanical behavior of marble exposed to freeze-thaw-fatigue loading. *Int J Rock Mech Min Sci* 138:104648. <https://doi.org/10.1016/j.ijrmmms.2021.104648>
- Tutuncu AN, Podio AL, Sharma MM (1998) Nonlinear viscoelastic behavior of sedimentary rocks, Part II: Hysteresis effects and influence of type of fluid on elastic moduli. *Geophysics* 63(1):195–203. <https://doi.org/10.1190/1.1444313>
- Wang Y, Feng WK, Hu RL, Li CH (2021) Fracture evolution and energy characteristics during marble failure under triaxial fatigue cyclic and confining pressure unloading (FC-CPU) conditions. *Rock Mech Rock Eng* 54(2):799–818. <https://doi.org/10.1007/s00603-020-02299-6>
- Xie K, Jiang D, Sun Z, Chen J, Zhang W, Jiang X (2018) NMR, MRI and AE statistical study of damage due to a low number of wetting–drying cycles in sandstone from the three gorges reservoir area. *Rock Mech Rock Eng* 51(11):3625–3634. <https://doi.org/10.1007/s00603-018-1562-6>
- Yang X, Han X, Liu E, Zhang Z, Wang X (2018) Experimental study on the acoustic emission characteristics of non-uniform deformation evolution of granite under cyclic loading and unloading test. *Rock Soil Mech* 39(8):2732–2739. <https://doi.org/10.16285/j.rsm.2018.0048>. (In Chinese)
- Yang S, Huang Y, Tang J (2020) Mechanical, acoustic, and fracture behaviors of yellow sandstone specimens under triaxial monotonic and cyclic loading. *Int J Rock Mech Min Sci* 130:104268. <https://doi.org/10.1016/j.ijrmmms.2020.104268>
- Yuan SC, Harrison JP (2006) A review of the state of the art in modelling progressive mechanical breakdown and associated fluid flow in intact heterogeneous rocks. *Int J Rock Mech Min Sci* 43(7):1001–1022. <https://doi.org/10.1016/j.ijrmmms.2006.03.004>
- Zhang K, Li N, Chen Y, Liu W (2020a) Evolution characteristics of strain field and infrared radiation temperature field during deformation and rupture process of fractured sandstone. *Rock Soil Mech* 41(S1):95–105. <https://doi.org/10.16285/j.rsm.2019.1013>. (In Chinese)
- Zhang K, Li N, Liu W, Xie J (2020b) Experimental study of the mechanical, energy conversion and frictional heating characteristics of locking sections. *Eng Fract Mech* 228:106905. <https://doi.org/10.1016/j.engfracmech.2020.106905>
- Zhang M, Dou L, Konietzky H, Song Z, Huang S (2020c) Cyclic fatigue characteristics of strong burst-prone coal: experimental insights from energy dissipation, hysteresis and micro-seismicity. *Int J Fatigue* 133:105429. <https://doi.org/10.1016/j.ijfatigue.2019.105429>
- Zhao K, Yang D, Gong C, Zhuo Y, Wang X, Zhong W (2020) Evaluation of internal microcrack evolution in red sandstone based on time-frequency domain characteristics of acoustic emission signals. *Constr Build Mater* 260:120405. <https://doi.org/10.1016/j.conbuildmat.2020.120435>
- Zheng Q, Liu E, Sun P, Liu M, Yu D (2020) Dynamic and damage properties of artificial jointed rock samples subjected to cyclic triaxial loading at various frequencies. *Int J Rock Mech Min Sci* 128:104243. <https://doi.org/10.1016/j.ijrmmms.2020.104243>
- Zhu L, Pei X, Cui S, Liang Y, Luo L (2019) Experimental study on dynamic damage and strength characteristics of rock with vein mass. *Chin J Rock Mech Eng* 38(05):900–911. [https://doi.org/10.13722/j.cnki.jrme.2018.1201\(InChinese\)](https://doi.org/10.13722/j.cnki.jrme.2018.1201(InChinese))
- Zhu L, Cui S, Pei X, Wang S, He S, Shi X (2021) Experimental investigation on the seismically induced cumulative damage and progressive deformation of the 2017 Xinmo landslide in China. *Landslides* 18(4):1485–1498. <https://doi.org/10.1007/s10346-020-01608-y>

Publisher's Note Springer Nature remains neutral with regard to jurisdictional claims in published maps and institutional affiliations.

Springer Nature or its licensor (e.g. a society or other partner) holds exclusive rights to this article under a publishing agreement with the author(s) or other rightsholder(s); author self-archiving of the accepted manuscript version of this article is solely governed by the terms of such publishing agreement and applicable law.